Vacuum birefringence in high-energy laser-electron collisions

B. King
*Centre for Mathematical Sciences, Plymouth University, Plymouth, PL4 8AA, United Kingdom**

N. Elkina
Arnold Sommerfeld Center for Theoretical Physics, Ludwig-Maximilians-Universität München, Theresienstraße 37, 80333 München, Germany†

(Dated: March 24, 2016)

Real photon-photon scattering is a long-predicted phenomenon that is being searched for in experiment in the form of a birefringent vacuum at optical and X-ray frequencies. We present results of calculations and numerical simulations for a scenario to measure this effect using multi-MeV photons generated in the collision of electrons with a laser pulse. We find that the birefringence of the vacuum should be measurable using experimental parameters attainable in the near future.

arXiv:1603.06946v1 [hep-ph] 22 Mar 2016

Shortly after the discovery of the positron [1], several authors suggested the possibility that real photons could scatter off one another through interaction with virtual electron-positron pairs [2]. First calculated for low- [3–5] and high-energy [6, 7] photons propagating in a constant electromagnetic background and later in plane-wave backgrounds [8, 9], recent advances in laser technology have generated much interest in discovering this effect in experiment [10–13]. That photons polarised parallel and perpendicular to the background polarisation have a different probability to scatter, is often referred to as *vacuum birefringence*. When the source of photons is a laser pulse, a signal of birefringence is predicted to be observable from the induced ellipticity in the pulse's field [14–19], the scattered photons' angular distribution [20–24] and parametric frequency shift [23, 25–29] (for a review, the reader is referred to [30–32]).

Experimental probes of vacuum birefringence have focussed exclusively on colliding photons with lab energies much less than the electron rest mass [10–13]. As the ellipticity scales linearly with photon flux, the high photon flux available for these parameters is beneficial for measurement. However, the cross-section for photon-photon scattering also scales with the sixth power of the centre-of-mass energy [33].

In the current letter we show that a different approach to measuring vacuum birefringence using multi-MeV rather than X-ray or optical photons yields a stronger signal of this long sought-after effect, at parameters that are achievable with today's experimental facilities. We substantiate our claim with analytical calculation and numerical simulation.

Birefringence of optical materials can be expressed by photons experiencing two different refractive indices, depending on how the photon's polarisation is aligned to the symmetry of the material's structure. When a real photon with wavevector k and phase $\phi = k\cdot x$ propagates in a linearly-polarised plane wave background of vanishing frequency with wavevector $\varkappa$, phase $\varphi = \varkappa\cdot x$ and gauge potential $A = a_1 g_1(\varphi) + a_2 g_2(\varphi)$ where $\varkappa\cdot a_{1,2} = a_1\cdot a_2 = 0$, the two vacuum refractive indices experienced by a photon are for polarisation directions [9]:

$$e^\mu_{1,2} = \frac{k\cdot\varkappa\, a^\mu_{1,2} - k\cdot a_{1,2}\,\varkappa^\mu}{k\cdot\varkappa\,\sqrt{-a^2_{1,2}}}. \tag{1}$$

($\hbar = c = 1$ unless occurring explicitly.) The locally-constant-field approximation (LCFA) of integrating the rate of constant-crossed-field (CCF) processes over the spacetime structure of a non-constant laser background is believed to be valid [34–36] when the classical intensity parameter $\xi = \sqrt{\alpha}\,|p\cdot F|/(m\,p\cdot\varkappa)$ [37] ($\alpha\approx 1/137$ is the fine-structure constant) fulfills $\xi \gg 1$. Choosing $g_2(\varphi) = 0$, for a photon counterpropagating with the background, e_1 (e_2) is parallel (perpendicular) to the background electric field. The refractive index experienced by photons in these polarisation eigenstates is $n_{1,2} = 1 + \delta n_{1,2}$ where [9]:

$$\delta n_{1,2}(\varphi) = \frac{-\alpha m^2}{3(k^0)^2}\int_4^\infty dv\,\frac{z(\varphi)(2v+1\mp 3)}{v\sqrt{v(v-4)}} f(z^{-1}(\varphi)), \tag{2}$$

$z = (\chi_k/v)^{2/3}$, $\chi_k = \sqrt{\alpha}\,|k\cdot F|/m^3$ is the quantum non-linearity parameter [34], F is the external-field Faraday tensor [38], m is the electron mass and $f(\cdot) = i\mathrm{Ai}(\cdot) + \mathrm{Gi}(\cdot)$ (Ai and Gi are Airy and Scorer functions of the first kind [39]). When $\chi_k \ll 1$, one finds from Eq. (2) that $\delta n_{1,2}(\varphi) \approx \alpha(11\mp 3)\chi_k^2/180\pi(k^0)^2$, agreeing with well-known literature values [40].

The polarisation e of a real photon propagating through the birefringent vacuum can be expressed in terms of a superposition of two linear polarisation eigenstates [33]:

$$e = \frac{1}{\sqrt{2Vk^0}}\left[\mathrm{e}^{i\phi_1}\cos\vartheta_0\; e_1 + \mathrm{e}^{i\phi_2}\sin\vartheta_0\; e_2\right], \tag{3}$$

* b.king@plymouth.ac.uk
† nina.elkina@physik.uni-muenchen.de

where V is volume, ϑ_0 is the initial polarisation angle of the photon with respect to e_1 and $\phi_{1,2}$ is the phase acquired by each polarisation component:

$$\phi_{1,2} = \phi(k^2 = 0) - \frac{(k^0)^2}{k \cdot \varkappa} \int_{\varphi_i}^{\varphi_f} dy \; \delta n_{1,2}(y), \qquad (4)$$

when the photon travels between external-field phases φ_i and φ_f. As the photon propagates, a phase difference develops between the polarisation components, implying that an initially linearly-polarised photon becomes increasingly elliptically-polarised. However, as this change is just a pure phase, the mod-square and hence the probability that the photon polarisation is measured in a given eigenstate, remains constant as it must for an eigenstate. Nevertheless, if the circular polarisation of a photon, which was initially linearly polarised at an angle ϑ_0 is measured after propagation in the birefringent vacuum, the probability $\mathsf{P}_\pm$ of it being in a *helicity* eigenstate $e_\pm = (e_1 \pm i e_2)/\sqrt{2}$ is:

$$\mathsf{P}_\pm = \frac{1}{2}\left[1 \pm U(\vartheta_0, \Delta\phi)\right], \qquad (5)$$

where $U(\vartheta_0, \Delta\phi) = \sin 2\vartheta_0 \sin\Delta\phi$ is the second Stokes parameter [33] and $\Delta\phi = \phi_2 - \phi_1$ is the phase lag induced by vacuum birefringence. Hence in a linearly-polarised background "helicity flipping" *does* occur [17, 18], unless the photon is prepared in a linear polarisation eigenstate. Measurement of a helicity flip in single photons should be contrasted with ongoing [11, 12] and planned [13] measurements of the ellipticity induced in the electromagnetic field of a laser wave, which is instead a collective effect on many photons.

No helicity flip occurs for photons generated in a polarisation eigenstate. Therefore the polarisation of the background used to generate photons must be different to the polarisation of the background in which the photons helicity-flip. To measure helicity-flipping in experiment, one could envisage a two-stage set-up in which the generation of high-energy photons and process of helicity-flipping are separated, such as depicted in Fig. 1. Stage I generates high-energy photons via

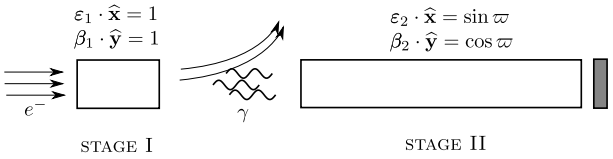

FIG. 1. A schematic of the envisaged two-stage set-up to measure vacuum birefringence in high-energy photons. $a_1 = (0, \boldsymbol{\varepsilon})$ and $a_2 = (0, \boldsymbol{\beta})$ are the polarisation directions of the external field in each stage.

nonlinear Compton scattering of electrons in an intense linearly-polarised counterpropagating laser pulse, and stage II collides the generated photons with a long counterpropagating laser pulse of linear polarisation rotated by ϖ in the plane of the first stage's polarisation. To demonstrate this set-up, we simulate both stages using the ANTARES particle-in-cell code that includes stochastic quantum effects using Monte Carlo methods, further details of which can be found in [41, 42].

By way of example for stage I, we simulate 2 GeV seed electrons counterpropagating with a laser pulse of frequency 1.55 eV (800 nm) and intensity parameter $\xi_1(\varphi) = \xi_1 \exp[-(\varphi/\sigma_1)^2] \; |\cos\varphi|$ for $\xi_1 = 100$ where $\sigma_1 = 8\pi$ (10.7 fs), with $\boldsymbol{\varepsilon}_1 = (1, 0, 0)$ and $\varkappa_1 = \varkappa^0(1, 0, 0, 1)$. The corresponding spectra and simulation dynamics are plotted in Fig. 2. 2000 unpolarised seed electrons generated a total of around 40000 photons with polarisations parallel to the eigenstates e_1 (12130 photons in the simulated spectrum in the plot, compared to 15740 from theory) or e_2 (3250 photons in the simulated spectrum in the plot, compared to 4740 from theory) via polarised nonlinear Compton scattering. The unpolarised photon spectrum

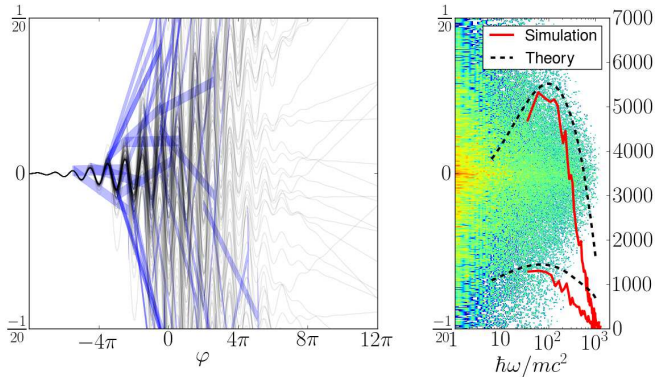

FIG. 2. Left: electrons (black) and photons (blue) produced in stage I of the simulation with $\varkappa^0 y/\pi$ as the vertical scale. Right: photon angular distribution (the left axis, with units k_y/π) and energy spectrum (the right axis, with units $\hbar\omega/mc^2$) of photons with polarisation e_1 (upper two curves) and e_2 (lower two curves).

expected from theory after stage I is:

$$\frac{\partial \mathsf{P}_\gamma(\chi_p, \chi_k)}{\partial \chi_k} = \int_{-\infty}^{\infty} d\varphi \; \frac{\partial \mathsf{R}_\gamma^{\mathsf{CCF}}[\chi_p(\varphi), \chi_k]}{\partial \chi_k}, \qquad (6)$$

where here $\chi_p = \chi_p(0)$ and $\mathsf{R}_\gamma^{\mathsf{CCF}}$ is the unpolarised rate per unit external-field phase for nonlinear Compton scattering in a constant crossed field. This is given by $\mathsf{R}_\gamma^{\mathsf{CCF}}(\chi_p, \chi_k) = (\mathsf{R}_\gamma^{\mathsf{CCF}}(\chi_p, \chi_k, e_1) + \mathsf{R}_\gamma^{\mathsf{CCF}}(\chi_p, \chi_k, e_2))/2$ for [43]:

$$\frac{\partial \mathsf{R}_\gamma^{\mathsf{CCF}}(\chi_p, \chi_k, e_{1,2})}{\partial \chi_k} = \frac{-\alpha}{\chi_p^2}\left\{\left[\frac{2 \pm 1}{z_\gamma} + \chi_k z_\gamma^{\frac{1}{2}}\right] \mathrm{Ai}'(z_\gamma) + \mathrm{Ai}_1(z_\gamma)\right\} \qquad (7)$$

where $\mathrm{Ai}_1(x) = \int_0^\infty \mathrm{Ai}(t + x) dt$ and $\partial \mathsf{R}_\gamma^{\mathsf{CCF}}(\chi_p, \chi_k)/\partial \chi_k$ refers to the polarisation average of the rate. The normalised cumulative distribution after stage I:

$$\mathsf{C}_\gamma(\chi_p, \chi_k) = \int_0^{\chi_k} \frac{\partial}{\partial \chi_k'} \frac{\mathsf{P}_\gamma(\chi_p, \chi_k')}{\mathsf{P}_\gamma(\chi_p)} \; d\chi_{k'} \qquad (8)$$

is plotted with the normalised cumulative distribution for a CCF in Fig. 3. This highlights the much broader spectrum of frequencies produced in the oscillating pulse of stage I when the CCF is integrated over.

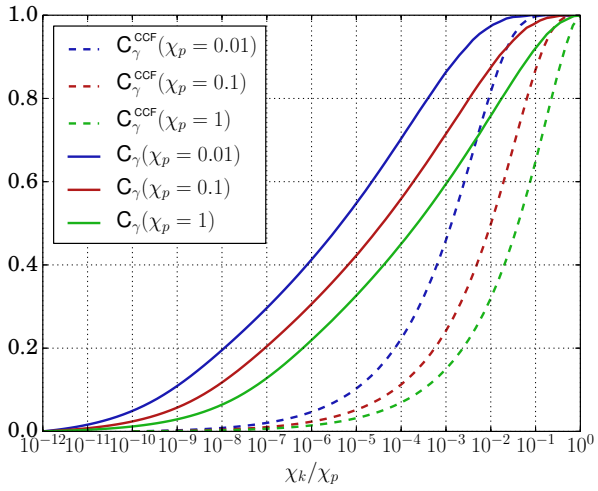

FIG. 3. The normalised cumulative distribution of photons at the end of stage I (solid lines) and the corresponding distribution in a CCF (dashed line).

The proportion of photons in polarisation eigenstates $e_{1,2}$ was determined by the ratio of the rates for nonlinear Compton scattering into those polarisations. The agreement with the spectrum produced in simulation is demonstrated by the dashed line in Fig. 2. In the theoretical estimate, electrons are assumed to counterpropagate with the laser pulse. If the transverse excursion, which is included in simulation and shown in the figure, is included in the estimate, the electron quantum nonlinearity parameter χ_p should on average be reduced, leading to a lower estimate of the spectrum of photons produced.

In order to describe the basic functionality of the simulation we follow the evolution of one event. In the event generator, we use three random numbers $0 < r_1, r_2, r_3$. At the beginning of each time step we first calculate the total unpolarised probability $\Delta t\, \partial \mathsf{P}_\gamma^{\mathsf{CCF}}(\gamma_p)/\partial t$ for an electron with gamma factor γ_p to produce an unpolarised photon over time interval Δt. A new photon is created if this probability is greater than r_1. Numbers r_2 and r_3 are then used to sample polarisation states and the energy of the secondary photon respectively. Which of the discrete polarisation states $\{e_1,\ e_2\}$ that is assigned to a photon is decided according to the relative expected abundance of each state: $\mathsf{P}_\gamma^{\mathsf{CCF}}(\gamma_p; e_1)/2\mathsf{P}_\gamma^{\mathsf{CCF}}(\gamma_p) \gtrless r_2$. The energy of a polarised photon k^0, is sampled from the normalised cumulative distribution by solving the following equation

$$\mathsf{C}_\gamma^{\mathsf{CCF}}(\gamma_p, \gamma_k; e) = r_3. \tag{9}$$

Unlike our previous work [42] we do not apply any

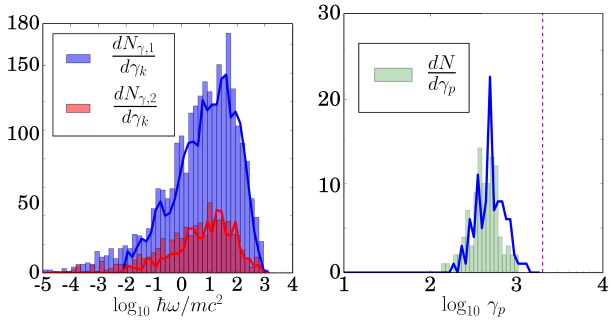

FIG. 4. Spectra obtained with the new event generator compared with stage I run for 100 initial electrons of energy 500 MeV, with $\xi_1 = 100$, $\sigma_1 = 8\pi$ and an initial electron offset of $z_0 = \sigma_1$. $N_{\gamma,1}$ ($N_{\gamma,2}$) refer to photons created in the e_1 (e_2) eigenstate. Bars (lines) plot values using the new (old) event generator. $N_{\gamma,1} = 2510$ (2020) and $N_{\gamma,2} = 687$ (513) for the new (old) event generator.

soft photon cutoff energy in calculations of singular integrals in corresponding probabilities. A new version of the event generator allows one to consider also soft photons by treating the weak singularity $\partial \mathsf{P}_\gamma(\gamma_p, \gamma_k; e)/\partial\gamma_k \sim \gamma_k^{-2/3}$ for $\gamma_k \ll \gamma_p$, by splitting the integration interval into soft and hard parts. The soft part is evaluated using a change of integration variable from γ_k to $\gamma_k^{1/3}$, which removes the apparent singularity. Further improvements implemented in accurate event generation routines will be described in [44]. Substantial improvement of the accuracy in QED simulation is a prerequisite for accurate predictions for proposals of future laser experiments. To illustrate this point we apply our new event generator for a collection of photon data from stage I. In Fig. 4 we compare new results with ones obtained using the event generator of [42]. It can be seen that although qualitatively the results are similar, the quantitative difference in photon yield approaches 25%.

Following stage I, the electrons are filtered out and only the high-energy photons remain, which then collide with a long laser pulse. To illustrate the phenomena involved, we consider a laser frequency of 1.55 eV (800 nm) and classical nonlinearity parameter $\xi_2(\varphi) = \xi_2\,\mathrm{sech}^2(\varphi/\sigma_2)\ |\cos\varphi|$ for $\xi_2 = 50$, $\sigma_2 = 8000\pi$ (10.7 ps) and wavevector $\varkappa_2 = \varkappa^0(1, 0, 0, 1)$. Crucially, this laser pulse is now polarised with electric-field vector $\boldsymbol{\varepsilon}_2 = (\sin\varpi, \cos\varpi, 0)$ and we choose $\varpi = -\pi/4$ to maximise helicity flipping. To simplify the analysis, we make the approximation that photons collide head-on with the laser background in stage II, which will turn out to be a good approximation for the parameters we are considering. We consider the asymmetry $\mathsf{P}_+ - \mathsf{P}_-$ to be the relevant experimental observable, which turns out to be exactly the second Stokes parameter $U(\Delta\phi)$ (since $\sin 2\vartheta_0 = -1$ for each photon in our discussion, from now on, we will suppress the ϑ_0 argument in U). From

Eq. (5) it is seen that this oscillates with propagation distance. Although photons in the e_1 (e_2) polarisation eigenstate will oscillate towards the negative (positive) helicity eigenstate e_- (e_+) by equal amounts, since more e_1 polarised photons are produced by stage I, the average ratio of each helicity eigenstate does not remain at 1/2 and so U does not remain at 0. The evolution of the Stokes parameter through stage II, is plotted in Fig. 5. As the photons begin to propagate through the background, the Stokes parameter increases monotonically for all frequencies. However, U oscillates over a shorter distance for higher frequency photons. This can be seen in by the more pronounced oscillation for higher photon frequencies in Fig. 5. When the Stokes parameter of the highest-frequency photons changes sign, the spectrum average $\langle U\rangle$ is no longer over terms of the same sign, the summation becomes incoherent and the effect saturates. No further increase in $\langle U\rangle$ is expected beyond this point. The average Stokes parameter measured after

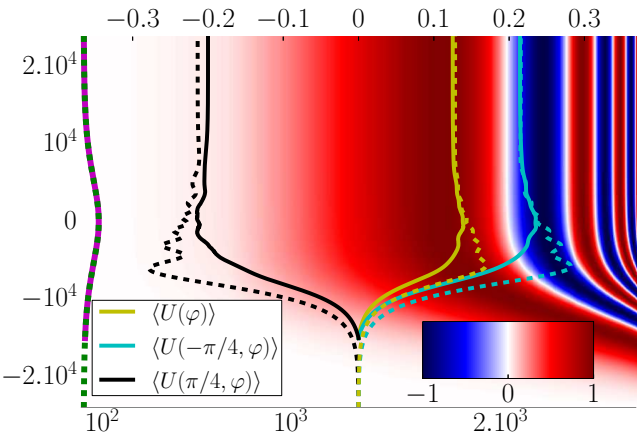

FIG. 5. Simulation and theory results for stage II of Fig. 1. At the end of stage II, simulation predicts $\langle U\rangle = 0.125$, theory predicts $\langle U\rangle = 0.128$. The vertical axis represents evolution in units of φ/π. The background colour signifies U for photon frequency given by the lower horizontal axis in units of the electron mass. The line along the left vertical axis is the shape of the laser background envelope. Dashed lines represent the calculations from theory, which assumes photons counter-propagate with the background, solid lines are results from simulation.

stage II is calculated from theory using:

$$\langle U\rangle(\chi_p) = \mathsf{A}_e(\chi_p)\int d\chi_k\; U[\Delta\phi(\chi_k)]\,\frac{\partial}{\partial\chi_k}\frac{\mathsf{P}_\gamma(\chi_p,\chi_k)}{\mathsf{P}_\gamma(\chi_p)}\,, \tag{10}$$

for post stage II values, where $\mathsf{A}_e(\chi_p) = (\mathsf{P}_\gamma(\chi_p, e_1) - \mathsf{P}_\gamma(\chi_p, e_2))/2\mathsf{P}_\gamma(\chi_p)$ is the asymmetry in the photon polarisation. The agreement with simulation and the effect of saturation is shown in Fig. 6. For the relevant case of $\chi_k \ll 1$, the phase difference has the simple form $\Delta\phi = \alpha\langle\chi_k\xi_2\rangle_\varphi/30\pi$, where $\langle f\rangle_\varphi = \int d\varphi\; f(\varphi)$. For the many-cycle pulse form of stage II, this becomes $\Delta\phi = \alpha\chi_k\xi_2\sigma_2/45\pi$. This implies in the lab system, the wavelength of oscillation of the Stokes' parameter λ_U is related to the wavelength of the individual photon λ by $\lambda/\lambda_U = (\alpha/30\pi)(E/E_{\rm cr})^2(1-\cos\theta)$. It can be seen that several parameters of stage II can be combined into the single invariant parameter $\Delta\phi_{\rm max} = \alpha\langle\chi_p\xi_2\rangle_\varphi/30\pi$, as plotted in Fig. 6. As $\langle U\rangle$ is a ratio of probabilities generated by integration over the spectrum and the pulse, this is independent of ξ_1 in the CCF. For the LCFA to be applicable, the pulse used in stage I must be many-cycle and hence $\langle U\rangle$ is also independent of σ_1 in the parameter range of interest. Remarkably, the single parameter $\Delta\phi_{\rm max}$ is sufficient for quantifying helicity-flipping for a large range of possible variables in the considered scenario. This allows one to be able to predict for what parameters $\langle U\rangle$ saturates and for what value, depicted in Fig. 6.

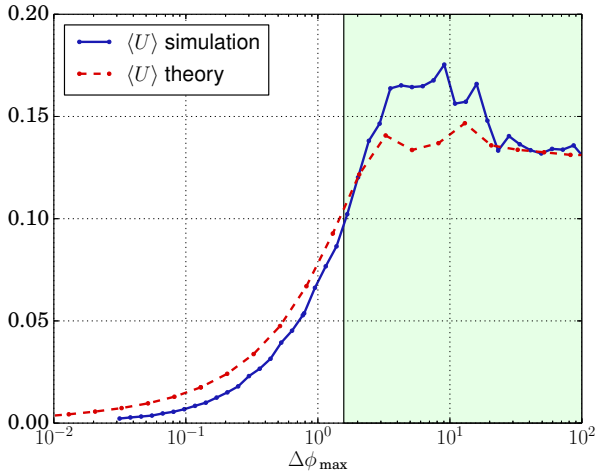

FIG. 6. Average Stokes parameter after stage II. Theory predicts saturation of the effect to begin in the shaded region.

One way of increasing the signal and the maximum value of the Stokes parameter is to use a much narrower-bandwidth source of high-energy photons. An example of this is to take a synchrotron as a source of high-energy photons, which has recently been analysed in [45]. Another possibility is to consider the stage I electrons to be produced at higher energies in a particle accelerator. By way of example we briefly consider this *accelerator-based* set-up, taking values of the order of those achieved at the Stanford Linear Accelerator E-144 experiment [46, 47] of 47 GeV electrons colliding with a 1.6 ps laser pulse of maximum intensity parameter $\xi_1 = 0.36$ at 527 nm wavelength. Since $\xi_1 \not\gg 1$ and the LCFA used in simulations is no longer valid [48], we estimate the photon spectrum using Eq. (6) with the unpolarised rate for nonlinear Compton scattering in a monochromatic background. The leading-order term in the perturbative ex-

pansion in ξ is [34]:

$$\frac{\partial \mathsf{R}_{\gamma}^{\mathrm{MONO}}(\chi_p,\chi_k,\xi,e_{1,2})}{\partial \chi_k} \approx \frac{\alpha\xi^2}{16\pi\chi_p^2}\left[2 \pm 1 + \frac{\chi_k^2}{\chi_p(\chi_p-\chi_k)}\right], \tag{11}$$

where the polarisation dependency is similar to the CCF case, $\chi_k \in [0, \chi_k^{\max}]$ and $\chi_k^{\max} = \chi_p[1+\xi(1+\xi^2/2)/2\chi_p]^{-1}$, which is integrated over the pulse envelope in stage I. For stage I, we consider a short pulse with $\xi_1 = 0.36$ and 15 fs duration and the same frequency as the E-144 experiment of 2.35 eV (527 nm wavelength). Apart from being considerably suppressed, the produced spectrum differs from the LCFA case ($\xi \gg 1$) in that the mean frequency and variance are both lower. As the spectrum is narrower, the value the Stokes parameter can reach before saturation is increased, as illustrated in Fig. 7. For example, if the laser employed in stage II was

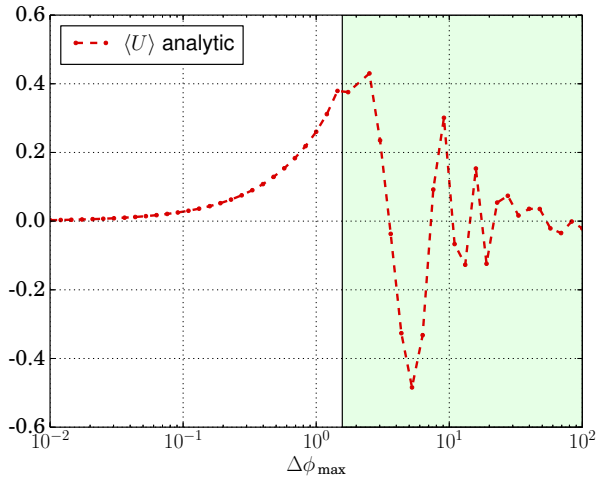

FIG. 7. Average Stokes parameter after stage II for the accelerator set-up with $\xi_1 = 0.36$, and $\sigma_1 = 17\pi$ (15 fs). The shaded region corresponds to where theory predicts the onset of saturation.

slightly longer than in E-144 at 10 ps ($\sigma_2 = 11350\pi$), and slightly stronger at $\xi_2 = 1$ then $\Delta\phi_{\max} = 0.57$ and $\langle U\rangle = 0.15$. This is comparable with the *laser-based* set-up considered previously, if the same χ_p value is taken and 700 MeV seed electrons collide with a $\xi_1 = 50$, $\sigma_1 = 8\pi$, 1.55 eV pulse in stage I, followed by photons propagating through a $\xi_2 = 20$, 5.4 ps ($\sigma_2 = 4000\pi$) pulse in stage II then $\langle U\rangle = 0.10$. Although these values for the Stokes parameters are of similar magnitude, the accelerator-based set-up considerably relaxes the requirement on the stage II laser.

The helicity of photons with energies $1-10$ MeV can be measured using Compton scattering on polarised atomic electrons in transmission polarimetry [49]. Furthermore, the creation of electron-positron pairs in an intense laser-pulse is also polarisation-dependent [50] and this form of polarimetry in a similar type of set-up for parameters at the ELI facility has been considered recently in more detail in [19].

When high-energy photons propagate through an intense electromagnetic background, they can undergo decay into electron-positron pairs [8]. These pairs would emit high energy photons and hence act as a background for the signal of photon-photon scattering. The expected number of pairs generated per electron in stage I via electron-seeded pair creation can be approximated for $\xi \gg 1$ using $\langle N_e\rangle = \sigma_1 \mathsf{R}_{\gamma e}(\chi_p)$ with the approximate rate $\mathsf{R}_{\gamma e}(\chi_p) = 3\alpha^2 \ln(1+\chi_p/12)\exp(-16/3\chi_p)(1+0.56\chi_p+0.13\chi_p^2)^{1/6}$ (adapted from [51]), giving $\langle N_e\rangle \approx 10^{-9}$ for the parameters considered in the laser-based set-up and is even lower for the accelerator-based set-up. For stage II, the probability per unit phase of pair creation for e_1 and e_2 polarised photons is $\mathsf{R}_e \sim [\alpha\sqrt{3}(2\mp 1)/8]\mathrm{e}^{-8/3\chi_k}$ respectively [50], which is also heavily suppressed for $\chi_k \ll 1$.

A further source of background is the nonlinear Compton scattering of any residual electrons in the synthetic vacuum of stage II. Although initially these electrons are effectively at rest and nonlinear Compton scattering is negligible since $\chi_p \ll 0.1$, they will be accelerated in the large field volume and could potentially mask the photon-photon scattering signal. For $\chi_p \ll 1$, the probability per unit phase of generating e_1 and e_2 polarised photons via nonlinear Compton scattering is [50] $\mathsf{R}_e = \alpha(5\pm 3)/2\sqrt{3}$. For the long phase lengths considered in stage II, the expected number of photons generated per residual electron will be larger than one. However, since χ_p is in general lower than in stage I, these background photons will have a much lower frequency. Using an IR frequency cutoff on the photon-polarisation measured would remove this source of background. An example density of residual electrons is that in the LHC beamline, which is of the order of $10^6\,\mathrm{cm}^{-3}$ [52].

To conclude, the use of high-energy photons, such as produced in the collision of electron beams and laser pulses, offers a method significantly more sensitive to vacuum polarisation than current optical and forthcoming X-ray probes. As a consequence, such experiments can be used to place more stringent limits on the mass and interaction strength of axion-like particles, WISPs (Weakly Interactive Sub-eV Particles) and other dark-matter candidates [53, 54]. With the ANTARES code, we have demonstrated how real photon-photon scattering can be included in QED-plasma simulations and displayed good agreement with theory. Furthermore, we have showcased a new event generator for nonlinear Compton scattering that is capable of including arbitrarily low energies of photons.

B. K. would like to acknowledge the hospitality of

N. Elkina and useful discussions with P. Böhl and A. Ilderton. This work was supported by the Grant No. SFB TR18 project B13 and the Arnold Sommerfeld Center for Theoretical Physics. Plots were generated with `Matplotlib` [55].

[1] C. D. Anderson, Phys. Rep. **3**, 491 (1933).
[2] O. Halpern, Phys. Rep. **44**, 855 (1934).
[3] H. Euler and B. Kochel, Naturwissenschaften **23**, 246 (1935).
[4] V. Weisskopf, Kgl. Danske Videnskab. Selskab, Mat.-fys. Medd. **14**, 6 (1936).
[5] W. Heisenberg and H. Euler, Z. Phys. **98**, 714 (1936).
[6] A. Akhieser, L. Landau, and I. Pomeranchook, Nature **138**, 206 (1936).
[7] A. Achieser, Phys. Z. Sov. **11**, 264 (1937).
[8] N. B. Narozhnyĭ, Sov. Phys. JETP **28**, 371 (1969).
[9] V. N. Baĭer, A. I. Mil'shteĭn, and V. M. Strakhovenko, Sov. Phys. JETP **42**, 961 (1976).
[10] D. Bernard et al., Eur. Phys. J. D **10**, 141 (2000).
[11] G. Zavattini et al., Int. J. Mod. Phys. A **27**, 1260017 (2012).
[12] A. Cadène, P. Berceau, M. Fouché, R. Battesti, and C. Rizzo, Eur. Phys. J. **D68**, 16 (2014), 1302.5389.
[13] H.-P. Schlenvoigt, T. Heinzl, U. Schramm, T. E. Cowan, and R. Sauerbrey, Physica Scripta **91**, 023010 (2016).
[14] T. Heinzl et al., Opt. Commun. **267**, 318 (2006).
[15] A. Di Piazza, K. Z. Hatsagortsyan, and C. H. Keitel, Phys. Rev. Lett. **97**, 083603 (2006).
[16] B. King, A. Di Piazza, and C. H. Keitel, Phys. Rev. A **82**, 032114 (2010).
[17] V. Dinu, T. Heinzl, A. Ilderton, M. Marklund, and G. Torgrimsson, Phys. Rev. D **89**, 125003 (2014), URL `http://link.aps.org/doi/10.1103/PhysRevD.89.125003`.
[18] V. Dinu, T. Heinzl, A. Ilderton, M. Marklund, and G. Torgrimsson, Phys. Rev. D **90**, 045025 (2014), URL `http://link.aps.org/doi/10.1103/PhysRevD.90.045025`.
[19] Y. Nakamiya, K. Homma, M. T., and K. Seto (2015), hep-ph/1512.00636.
[20] B. King, A. Di Piazza, and C. H. Keitel, Nature Photon. **4**, 92 (2010).
[21] Y. Monden and R. Kodama, Phys. Rev. Lett. **107**, 073602 (2011).
[22] G. Y. Kryuchkyan and K. Z. Hatsagortsyan, Phys. Rev. Lett. **107**, 053604 (2011).
[23] B. King and C. H. Keitel, New J. Phys. **14**, 103002 (2012).
[24] F. Karbstein, H. Gies, M. Reuter, and M. Zepf, Phys. Rev. D **92**, 071301 (2015), URL `http://link.aps.org/doi/10.1103/PhysRevD.92.071301`.
[25] E. Lundström et al., Phys. Rev. Lett. **96**, 083602 (2006).
[26] H. Gies, F. Karbstein, and R. Shaisultanov, Phys. Rev. D **90**, 033007 (2014), URL `http://link.aps.org/doi/10.1103/PhysRevD.90.033007`.
[27] B. King, P. Böhl, and H. Ruhl, Phys. Rev. D **90**, 065018 (2014).
[28] P. Böhl, B. King, and H. Ruhl, Phys. Rev. A **92**, 032115 (2015), URL `http://link.aps.org/doi/10.1103/PhysRevA.92.032115`.
[29] H. Gies, F. Karbstein, and N. Seegert (2016), arXiv:1603.00314.
[30] M. Marklund and P. K. Shukla, Rev. Mod. Phys. **78**, 591 (2006).
[31] A. Di Piazza et al., Rev. Mod. Phys. **84**, 1177 (2012).
[32] B. King and T. Heinzl, High Power Laser Science and Engineering **4**, e5 (2016), hep-ph/1510.08456.
[33] V. B. Berestetskii, E. M. Lifshitz, and L. P. Pitaevskii, *Quantum Electrodynamics (second edition)* (Butterworth-Heinemann, Oxford, 1982).
[34] V. I. Ritus, J. Russ. Laser Res. **6**, 497 (1985).
[35] B. King and H. Ruhl, Phys. Rev. D **88**, 013005 (2013).
[36] C. N. Harvey, A. Ilderton, and B. King, Phys. Rev. A **91**, 013822 (2015).
[37] T. Heinzl and A. Ilderton, Opt. Commun. **282**, 1879 (2009).
[38] J. D. Jackson, *Classical Electrodynamics* (John Wiley & Sons, Inc., New York, 1975).
[39] O. Valleé and M. Soares, *Airy Functions and Applications to Physics* (Imperial College Press, 57 Selton Street, Covent Garden, London WC2H 9HE, 2010).
[40] R. Baier and P. Breitenlohner, Acta Phys. Austriaca **25**, 212 (1967).
[41] E. N. Nerush et al., Phys. Rev. Lett. **106**, 035001 (2011).
[42] N. V. Elkina et al., Phys. Rev. ST Accel. Beams **14**, 054401 (2011).
[43] A. I. Nikishov and V. I. Ritus, Sov. Phys. JETP **19**, 529 (1964).
[44] N. V. Elkina, *In preparation* (2016).
[45] A. Ilderton and M. Marklund (2016), hep-ph/1601.08045.
[46] D. L. Burke et al., Phys. Rev. Lett. **79**, 1626 (1997).
[47] C. Bamber et al., Phys. Rev. D **60**, 092004 (1999).
[48] V. Dinu, C. Harvey, A. Ilderton, M. Marklund, and G. Torgrimsson, Phys. Rev. Lett. **116**, 044801 (2016).
[49] G. Alexander et al., Nucl. Instrum. Meth. A **610**, 451 (2009), URL `http://www.sciencedirect.com/science/article/pii/S016890020`
[50] B. King, N. Elkina, and H. Ruhl, Phys. Rev. A **87**, 042117 (2013).
[51] V. N. Baier, V. M. Katkov, and V. M. Strakhovenko, Soviet Phys. Nucl. Phys **14**, 572 (1972).
[52] Brumfiel, G., Nature (2008), URL `http://www.nature.com/news/2008/080905/full/news.2008.1085.`
[53] S. Villalba-Chávez and C. Müller, JHEP **06**, 177 (2015).
[54] H. Hu and J. Huang, Phys. Rev. A **90**, 062111 (2014), URL `http://link.aps.org/doi/10.1103/PhysRevA.90.062111`.
[55] J. D. Hunter, Computing In Science and Engineering **9**, 90 (2007).